JACS
JOURNAL OF THE AMERICAN CHEMICAL SOCIETY
Article
pubs.acs.org/JACS

# Organometallic Single-Molecule Electronics: Tuning Electron Transport through X(diphosphine)$_2$FeC$_4$Fe(diphosphine)$_2$X Building Blocks by Varying the Fe−X−Au Anchoring Scheme from Coordinative to Covalent

Franziska Lissel,[†] Florian Schwarz,[‡] Olivier Blacque,[†] Heike Riel,[‡] Emanuel Lörtscher,*[,‡] Koushik Venkatesan,*[,†] and Heinz Berke*[,†]

[†]Department of Chemistry, University of Zurich, Winterthurerstrasse 190, CH-8057 Zürich, Switzerland
[‡]Science & Technology Department, IBM Research - Zurich, Säumerstrasse 4, CH-8803 Rüschlikon, Switzerland

Supporting Information

**ABSTRACT:** A series of X(depe)$_2$FeC≡C−C≡CFe(depe)$_2$X complexes (depe =1,2-bis(diethylphosphino)ethane; X = I **1**, NCMe **2**, $N_2$ **3**, $C_2H$ **4**, $C_2SnMe_3$ **5**, $C_4SnMe_3$ **6**, NCSe **7**, NCS **8**, CN **9**, SH **10**, and $NO_2$ **11**) was designed to study the influence of the anchor group on organometallic molecular transport junctions to achieve high-conductive molecular wires. The $FeC_4Fe$ core is electronically functional due to the redox-active Fe centers and sp-bridging ligands allowing a strong electronic delocalization. **1**−**11** were characterized by elemental analyses, X-ray diffraction, cyclic voltammetry, NMR, IR, and Raman spectroscopy. DFT calculations on model compounds gave the HOMO/LUMO energies. **5**−**9** were investigated in mechanically controllable break-junctions. For **9**, unincisive features at $8.1 \times 10^{-7}$ $G_0$ indicate that sterical reasons prevent stable junctions to form or that the coordinative binding motif prohibits electron injection. **7** and **8** with the hitherto unexploited coordinatively binding end groups NCSe and NCS yielded currents of $1.3 \times 10^{-9}$ A (**7**) and $1.8 \times 10^{-10}$ A (**8**) at ±1.0 V. The $SnMe_3$ in **5** and **6** splits off, yielding junctions with covalent C−Au bonds and currents of $6.5 \times 10^{-7}$ A (**Au**−**5′**−**Au**) or $2.1 \times 10^{-7}$ A (**Au**−**6′**−**Au**). Despite of a length of almost 2 nm, the **Au**−**5′**−**Au** junction reaches 1% of the maximum current assuming one conductance channel in quantum point contacts. Additionally, the current noise in the transport data is considerably reduced for the covalent C−Au coupling compared to the coordinative anchoring of **7**−**9**, endorsing C−Au coupled organometallic complexes as excellent candidates for low-ohmic molecular wires.

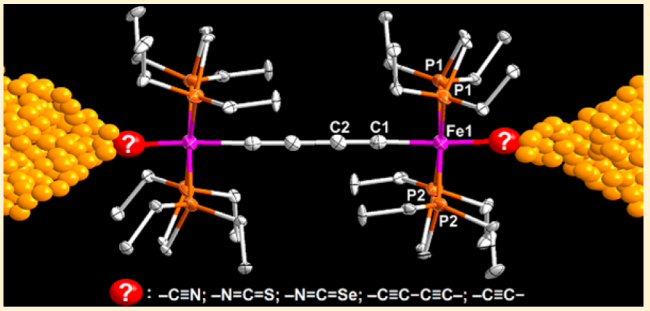


## INTRODUCTION

The field of molecular electronics aims at employing intrinsic molecular functionalities for specific electronic operations.[1−4] Electronic transport through molecular junctions depends on the chemical structure of the molecules, which however is hard to predict in such a solid-state type-of-device,[5] as the properties of the isolated molecule change substantially when it is coupled to metal leads. Nonetheless the evolution of atomic and molecular manipulation and molecular electronics has strongly progressed and gained momentum through interdisciplinary efforts, joining forces of theory, physics and chemistry.[6] From the chemistry side, the main contribution toward single-molecule electronics is to provide a rational design for the synthesis of unique molecular entities suitable of probing structure−function relationships,[7−9] which is a categorical prerequisite to comprehensively understand the processes underlying electronic transport on the single-molecule level.

Ultimately this know-how is expected to be the basis for creating tailored functional molecular building blocks for specific electronic tasks, as e.g. conductance switching, and eventually enabling the implementation of single-molecule devices to provide novel functionalities based on intrinsic molecular mechanisms, such as multilevel redox activity. A molecular transport junction can be divided into three main parts:[10] an experimental setup providing atomic-sized electrodes separated by a tunable gap of molecular dimensions (0−3 nm), a (functional or passive) molecular backbone providing a pathway for electrons to travel between the two electrodes under an applied field, and the termini of the molecular unit, the so-called end groups. These end groups establish the mechanical and electronic contact between the backbone and the electrodes by chemical means, thereby immobilizing the molecule in the junction to form a solid-state device. Suitable molecular entities are structurally rigid and consist of molecular orbitals (MOs) that are ideally coupled in an overlapping way along the

Received: August 2, 2014
Published: September 18, 2014

   dx.doi.org/10.1021/ja507672g | J. Am. Chem. Soc. 2014, 136, 14560−14569

electronic pathway to facilitate electron transport. The junction's conductance can now be modulated by varying the level of MO coupling, the energetic position of the MOs in respect to the Fermi energy, $E_F$, of the electrodes and the injection barriers from the electrodes to the MOs. In that context, the end groups are key to establish a mechanically stable contact and to control the electronic coupling between the molecule and the electrodes.[11] The molecular topologies are expected to determine the type of transport mechanism and its efficiency, namely the anchor group to determine the charge injection barrier and the molecular orbitals the pathways for electrons to tunnel through. Whereas the experimental techniques to investigate molecular transport are evolving at a fast pace and enable meanwhile even measurements at the single-molecule level, the number of suitable homologous series of molecules for a systematic study of the structure−function relationship is rather limited. Also, the conductance of commonly used purely organic molecules for single-molecule electronics is reported to be rather low and to decay generally exponentially with increasing molecular length until, at a certain length, the hopping-based low-conductance regime is reached. This constrains severely the dimensions of the molecular systems,[12−15] in particular to achieve long wires, and complicates the implemention of intrinsic molecular functionalities.

To achieve high conductance at relatively low bias for energy-efficient applications, the positions of the energy levels of the MOs need to be aligned with $E_F$ for resonant transport to occur through MOs. In contrast to purely organic entities, where MO and $E_F$ levels are usually energetically separated by several eV (in the isolated case), organometallic compounds enable a facile tuning of the MO energies, because of their strong dependence on the kind of the metal center.[16−20] The design and synthesis of the Creutz−Taube[21] ion furthermore established that an organic ligand connecting two or more redox-active metal cores allows a delocalized electronic system to be formed between the metal centers which act as an intramolecular electron pathway for transport. Additionally, the insertion of redox-active metal centers into organic frameworks, termed "relay approach", was shown to improve the molecular conductance of the entire framework by providing defined donor−acceptor sites.[22]

In recent years, organometallic complexes of the type (Cp*)(PP)MC$_n$M(PP)(Cp*) (Cp* = $\eta^5$-C$_5$Me$_5$, P = monodentate phosphine ligand or PP = bidentate phosphine ligand, C$_n$ organic bridging ligand) were intensively employed to study intramolecular charge transport.[23−25] The covalently bonded and electronically delocalized bridge poses a structurally well-defined rigid-rod electron pathway, whereas the options to alter the incorporated metal centers,[26,27] the bridging[28,29] and nonbridging ligands[30] in order to vary the MO alignment open the possibility to gain in-depth understanding of the electronic processes taking place at the molecular level. Electrochemical and spectroscopic experiments evidenced that the electronic delocalization can extend over the entire length of the organometallic unit.[31−33] The reversibility of the intramolecular redox process was found to be highest for the unsaturated, rigid-rod type and electronically versatile C$_4$ ligand and decreased dramatically if other types of sp/sp$^2$ systems were employed.[28,29,34−36] Among the C$_4$-bridged bimetallic systems, the homonuclear (Cp*)(PP)FeC$_4$Fe(PP)(Cp*) class is highlighted by an exceptionally large charge delocalization and a high stabilization of the oxidized species.[27,37−39] First experimental evidence suggests that spectroelectrochemical data derived from solution-based bulk measurements can tentatively be related to the electronic properties expressed on a single-molecule level.[40] Despite this, single-molecule transport measurements of compounds of the (PP)MC$_n$M(PP) class are rare, as the design and realization of organometallic fragments with open terminal sites that would allow for the insertion of electrode binding end groups constitute significant synthetic challenges. Up to date, only a mononuclear ruthenium[41] and platinum[42] complex as well as selected di- and trinuclear ruthenium entities[8,43−45] were investigated. Another experimental challenge is the required backbone length. As the direct electron tunneling between the Au electrodes is a non-negligible conductance channel in a molecular junction,[46] the electrode spacing of the corresponding metal−molecule−metal system has to be taken into account when comparing molecular conductances in general and molecule−metal coupling strengths in particular. As the direct electron tunneling contribution is strong for short electrode separations, longer compounds are better suited for such comparative studies, adding to synthetic challenges. Hence, the rich ligand chemistry and the high tunability of transition metals, which make the (PP)MC$_n$M(PP) class very attractive for molecular electronic applications, is so far not sufficiently exploited and needs further chemical realization and physical transport experiments.

We recently reported the stepwise assembly of a homometallic tetranuclear Me$_3$SiC$_4${Fe}C$_4${Fe}C$_4${Fe}C$_4${Fe}C$_4$SiMe$_3$ ({Fe} = Fe(depe)$_2$, depe = 1,2-bis(diethylphospino)ethane) unit, which showed extensive charge delocalization and vibrational coupling over the entire unsaturated organometallic backbone.[34] Based on these findings, we targeted to attach electrode-binding terminal groups to the {Fe}−C≡C−C≡C−{Fe} unit, thus combining the favorable properties of the Fe(II) core(s) with those of the butadiyne bridging ligand while realizing molecular junctions in the length range of 1.3−2.0 nm to reduce the direct electron tunneling contribution.

Toward this end, we first designed a triad of organometallic precursors of the type X{Fe}C$_4${Fe}X (X = I **1**,[34] NCMe **2**, and N$_2$ **3**) with reactive terminal ligands X. Starting from these source compounds, synthetic strategies were devised to modify the end groups for contact to Au electrodes. Using different synthetic pathways, we capped the central {Fe}C$_4${Fe} unit with X = C≡CH **4**, C≡CSnMe$_3$ **5**, C$_4$SnMe$_3$ **6**,[34] NCSe **7**, NCS **8**, CN **9**, SH **10**, and NO$_2$ **11** to study the influence of molecule−metal coupling on the transport properties. The **4**−**11** series of complexes consists of principally two different types of electrode-binding molecules. Those with terminal H atoms or Me$_3$Sn moieties attach to the Au surface by elimination of these moieties, forming junctions with X = C$_2$ (**5′**) or X = C$_4$ (**6′**). **5′** and **6′** are expected to establish covalent bonds to the Au surface, while complexes with Lewis basic end groups (**7**−**9** and **11**) form coordinative bonds. It seems reasonable to expect that the utilization of covalent C−Au bonds will lead to an increased stability of the molecular junction compared to the coordinative bonding case. Moreover, a stronger MO overlap due to the shorter electrode−molecule distance and therefore a higher overall conductance is anticipated for C−Au bonds. The presently best conducting molecular wires are those with poly *p*-phenylene junctions possessing also a direct C−Au binding.[47] Here, tunneling between the distinct $\pi$-system of the phenyls mediates transport, whereas in our case a delocalized electron system enables electron transport between the metal centers.

To achieve resonant transport, the MOs of the molecule have to be aligned to $E_F$, so that the electronegativity is similar. It was


dx.doi.org/10.1021/ja507672g | J. Am. Chem. Soc. 2014, 136, 14560−14569

**Scheme 1. Reaction Pathways to Modify the Terminal X Functional Group of the X{Fe(depe)$_2$}C$_4${Fe(depe)$_2$}X Unit**

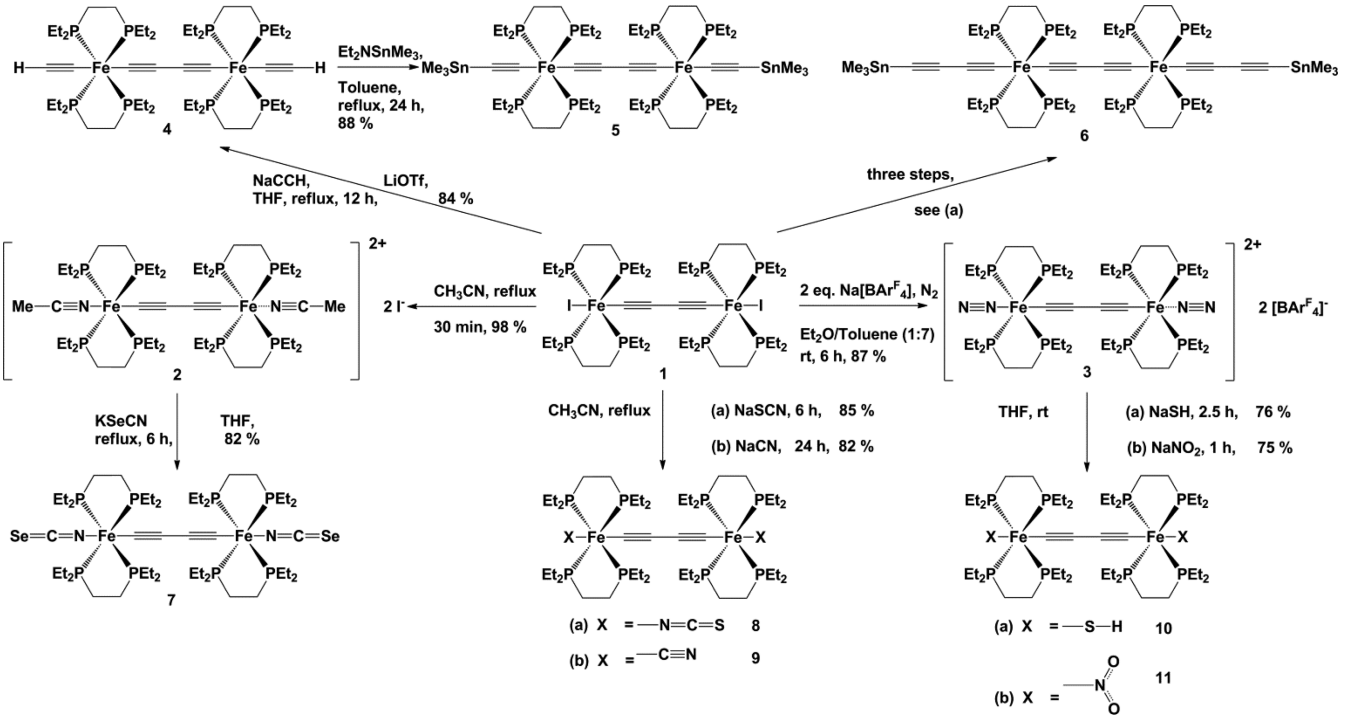


[a]Three step synthesis.[34] [BAr$^F_4$]$^-$ = tetrakis[(3,5-trifluoromethyl)phenyl]borate.

shown that Au electrodes are comparably soft according to the HSAB concept developed by Pearson.[48] The same concept states that the chemical hardness can be correlated to the energy difference between the highest occupied molecular orbital (HOMO) and the lowest unoccupied molecular orbital (LUMO), called the HOMO−LUMO gap $\Delta E_{(H-L)}$, and allows the strength of donor−acceptor interactions to be predicted.[49] A small HOMO/LUMO gap means soft, and a large HOMO/LUMO gap means hard in character, while the Mulliken electronegativity $(I + A)/2$ ($I$ = ionization potential, $A$ = electron affinity) at high negative energies means high electronegativity and vice versa. Following this line of thought, molecules prone for high resonant conductivity should be soft in character and have a relatively low electronegativity to adjust to $E_F$ of the Au electrodes. To gain insight into the influence of the terminal groups on the energetic regime of the molecular orbitals, the molecular geometries of selected model complexes **5**-Me, **6**$_H$-Me, **7**-Me, **8**-Me, **9**-Me, **10**-Me, and **11**-Me were optimized at the PBE1PBE/LANL2DZ level, and the HOMO/LUMO energies and chemical hardnesses of the compounds were obtained by single-point calculations with the 6-311+g(d) basis set and the same PBE1PBE functional.

All terminal substituents chosen possess a conjugation scheme that allows charge delocalization of the central {Fe}C$_4${Fe} unit to be extended over the molecule−metal interfaces. The strong electronic delocalization, the relatively high chemical stability, and the rigid-rod conjugated structures make a possible deployment of the {Fe}C$_4${Fe} unit attractive for applications as molecular wires. While cyanide,[50] isocyanide,[51] thiol,[52,53] and nitro substituents[8] are frequently employed as end groups, sp carbons are as yet rarely used,[7,54,55] and the utilization of NCS and NCSe as end groups is, to the best of our knowledge, unprecedented in molecular electronics. The affinity of S toward Au is well established, and one can reasonably assume that replacing S with the softer Se could enhance the orbital interaction of the soft Au electrode and the anchor groups[56] and additionally reinforce the stability of the formed junction. As mentioned before, capping a carbon function with either trimethylsilyl[57] or trimethylstannyl[58] substituents allows strong C−Au $\sigma$-bonds to be established after deprotection of the EMe$_3$ group (E = Si, Sn). The utilization of trimethylstannyl groups is preferable since due to the weaker Sn−C bond the cleavage of the C−Sn bonds occurs spontaneously at the electrodes and pre-experiment deprotection by a suitable reagent is not required. The linear structure, rigidness, and orbital arrangement of sp-hybridized C make these end groups highly interesting for the investigation of molecular transport.[54,55,59]

## EXPERIMENTAL SECTION

**Syntheses and Spectroscopic Characterizations.** All experiments and measurements were carried out under a dinitrogen atmosphere using Schlenk techniques or in a glovebox (M. Braun 150B-G-II). All compounds were worked up to an analytically pure state without the use of column chromatography. The experimental part containing the description of the syntheses, one- and two-dimensional NMR experiments (Figures S1−S28), IR (Figures S29−S38) and Raman data (Table S1), and cyclic voltammetry experiments at different scan rates (Figures S42−S50) as well as the results of the elemental analyses can be found in the Supporting Information.

**X-ray Structure Analyses.** The molecular structures of complexes **5**, and **7**−**9** are depicted in Figure 2. The dicationic complexes [**2**]$^{2+}$ and [**3**]$^{2+}$ are illustrated in Figure S39, and the molecular structures of the compounds **5**, **10** and **11** are shown in Figure S40. Selected bond lengths, intramolecular distances, and angles are summarized in Table S2. The data collection and structure-refinement data for compounds **2**, **3**, and **5**−**11** are presented in Tables S3−S5. Single-crystal X-ray diffraction data were collected at 183(2) K on a Xcalibur diffractometer (Ruby CCD detector) or on a SuperNova area-detector diffractometer (for **6**), using a single wavelength enhance X-ray source with MoK$_\alpha$


dx.doi.org/10.1021/ja507672g | J. Am. Chem. Soc. 2014, 136, 14560−14569

radiation ($\lambda$ = 0.71073 Å).[60] The selected suitable single crystals were mounted using polybutene oil on the top of a glass fiber fixed on a goniometer head and immediately transferred to the diffractometer. Pre-experiment, data collection, data reduction, and analytical absorption corrections[61] were performed with the program suite CrysAlis$^{Pro}$.[60] Using WinGX[62] or Olex,[63] the crystal structures were solved with SHELXS97[64] using direct methods, and the structure refinements were performed by full-matrix least-squares on $F^2$ with SHELXL97[64] for **3**, **5**, **8**–**11** and SHELXL2013[64] for **2**, **4** and **7**. PLATON[65] was used to check the results of the X-ray analyses. For more details about the refinements, see the Supporting Information and/or the refine_special_details and iucr_refine_instructions_details sections in the Crystallographic Information files (Supporting Information). CCDC-986825 (for **2**), CCDC-986826 (for **3**), CCDC-986827 (for **4**), CCDC-986828 (for **5**), CCDC-986829 (for **7**), CCDC-986830 (for **8**), CCDC-986831 (for **9**), CCDC-986832 (for **10**), and CCDC-986833 (for **11**) contain the supplementary crystallographic data for this paper. These data can be obtained free of charge from The Cambridge Crystallographic Data Center via www.ccdc.cam.ac.uk/data_request/cif.

**Computational Details.** DFT calculations were performed with the Gaussian03 program package[66] using the hybrid functional PBE1PBE[67] in conjunction with the LanL2DZ basis set[68−70] for the geometry optimizations and with the 6-311+G(d) basis set[71−73] on all atoms for the determination of the energy levels. Geometries were optimized with a $C_i$ (inversion center) or a $C_2$ (2-fold axis) symmetry, and the ethyl groups of the depe ligands were replaced by methyl groups. The results are summarized in Table 3 and Figure S51.

**Single-Molecule Transport Measurements.** Transport measurements were taken at 300 K under ultrahigh vacuum conditions (pressure <2 × $10^{-9}$ mbar) by repeated opening and closing of the molecular junction using a three-point bending mechanism upon simultaneous current−voltage ($I$−$V$) data acquisition[74] using a Hewlett-Packard HP4156B Parameter Analyzer with 1 fA current resolution. After initial breaking of the Au−Au junction, the dinuclear Fe compounds were deposited onto the open junction from a 4 × $10^{-5}$ mol/L solution in tetrahydrofuran (THF), forming a submonolayer coverage on the two Au surfaces by the various bonding motifs. After evaporation of the solvent, the junction is slowly and stepwise closed until an electrical resistance of 1 MΩ at 1.2 V is being measured. Then the junction is opened again until a resistance of 3 TΩ at 1.2 V is reached, indicating a fully opened junction. In the subsequent opening and closing cycles, molecules can bridge the two electrodes, and metal−molecule−metal junctions are formed repeatedly. Statistical analysis, typically covering several hundred $I$−$V$ curves during junction forming and breaking events, is performed to identify the most probable transport characteristics[74] during this mechanical manipulation procedure.

## EXPERIMENTAL RESULTS

**Synthesis and Spectroscopic Properties of the Different Dinuclear Complexes.** Mononuclear iron complexes of the type $Fe(PP)_2X_2$ (PP = bidentate phosphine ligand, X = Cl, Br, I) are known to react with organic nitriles yielding the mono- or dinitrile coordinating complexes[75,76] as well as allowing the abstraction of the terminal halides by sterically hindered bases to obtain the corresponding dinitrogen complexes.[77] The dinuclear I{Fe}$C_4${Fe}I complex **1** (Scheme 1) is easily accessible and allows a facile substitution of the terminal iodo functions.[34] We targeted the dinuclear bis-nitrile (**2**) and bis-dinitrogen (**3**) species as synthetic intermediates to assemble a triad of reactive precursors to access entities based on the {Fe}$C_4${Fe} motif, which terminal functional groups are chemically "tunable". The di-iodo complex **1** reacted with refluxing acetonitrile to give the bis-acetonitrile coordinated dinuclear complex [**2**] as the di-iodo salt in very high yield (98%, Scheme 1). Treating **1** with two equivalents of sodium tetrakis[(3,5-trifluoromethyl)phenyl]borate under a dinitrogen atmosphere and apolar conditions gave the bis-dinitrogen complex [**3**] as the tetrakis[(3,5-trifluoromethyl)phenyl]-borate salt in good yield (87%, Scheme 1). The reaction of mononuclear (Cp*)(PP)FeCl and $Fe(PP)_2Cl_2$ cores with lithium acetylide[78] and sodium acetylide[79,80] reagents is well established. In a previous paper we could show that by reacting **1** with a freshly prepared lithiated $[C_4]^{2-}$ unit and subsequent deprotection and stannylation of the termini, the $C_4SnMe_3$ capped dinuclear complex **6** is accessible.[34] In a similar fashion the reaction of **1** with sodium acetylide in the presence of lithium triflate gave the acetylide capped compound **4**, which was stannylated using $NEt_2SnMe_3$ to yield the $C_2SnMe_3$ capped complex **5** (Scheme 1). Both compounds were isolated in good yields of 84% and 88%, respectively. The signal of the acetylenic proton of **4** in the $^1$H NMR appears as a quintet at 1.03 ppm due to a $^4J_{H-P}$ coupling with the four phosphorus atoms of the depe ligand (see Figure S10 for the $^1$H and $^1$H {$^{31}$P} spectra as well as Figure S13 for the P,H correlation spectrum). The stannylation to give **5** has a distinct influence on the spectroscopic properties (see NMR and IR parts of the Supporting Information), most notably on the $^{13}$C{$^1$H} resonance of the $C_\alpha$ carbon atom of the terminal acetylide group, which experiences a considerable low-field shift from 129.9 ppm for **4** to 170.2 ppm for **5**. Despite the stannyl substituent, the signal of the $C_\beta$ atom is likewise shifted low-field, albeit to a lesser extent, from 99.4 to 111.6 ppm (for **4** and **5**, respectively). In the $^{119}$Sn{$^1$H} NMR, the trimethyltin group of **5** appears as a quintet at −121.0 ppm due to the $^4J_{Sn-P}$ coupling (Figure S18). Compared to the corresponding singlet of the $C_4SnMe_3$ capped **6**, which is found at −36.3 ppm,[34] the signal is shifted considerably toward the lower field.

Starting from the bis-acetonitrile complex $[\mathbf{2}]^{2+}$ and using KSeCN as a reagent, the isoselenocyanate capped complex **7** was obtained in good yield (82%, Scheme 1).

In a similar line, reacting the di-iodo complex **1** in refluxing acetonitrile with NaSCN and NaCN yielded the isothiocyanate capped **8** and the cyanide substituted complex **9** in good yields of 85% and 82%. *In situ* $^{31}$P{$^1$H} NMR measurements indicated the formation of the bis(acetonitrile) substituted $[\mathbf{2}]^{2+}$ as an intermediate. **7** and **8**, which differ from each other solely in the heteroatom of the terminal function, show a distinct consistency in their respective spectroscopic properties (Table 1 and Supporting Information).

**Table 1. IR and Raman $\nu(C_4)$ Bands of the Bridging Butadiyne Unit of Compounds 2−10**

| compd. | IR [cm$^{-1}$] $\nu_{as}(C_4)$ | Raman [cm$^{-1}$] $\nu_s(C_4)$ |
|---|---|---|
| **2** | 1946 (m) | 2088(s) |
| **3** | 2109 (m) | 2122(vs) |
| **4** | 1952 (w) | 2098(s) |
| **5** | 1936 (vs) | 2086(s) |
| **6**[b] | 1951 (m) (sh at 1967)[a] | 2102(vs) |
| **7** | 1950 (m) | 2097(vs) |
| **8** | 1950 (m) | 2097(vs) |
| **9** | 1955 (m) | 2103(vs) |
| **10** | 1940 (m) | 2094(s) |
| **11** | 1956 (m) | 2098(s) |

[a] $\nu(C_2)$. [b] Described in literature.[34]

The thiol and nitro capped dinuclear compounds **10** and **11** were obtained in yields of 74% and 75% (Scheme 1) by reacting the bis-dinitrogen complex $[\mathbf{3}]^{2+}$ with the corresponding sodium salts at room temperature, indicative of the facile replacement of the coordinated dinitrogen ligands. The bis-thiol compound **10** is prone to decomposition in solution or in air, apparently under oxidative conditions, presumably resulting in the formation of dithio bridged compounds. In the $^1$H NMR, the SH group gives rise to a quintet due to the $^3J_{H-P}$ coupling with the four phosphorus atoms of the depe ligand and is shifted considerably upfield to −6.34 ppm (Figure S25). For the ligand exchange reactions, an intermediate $[\{Fe\}{\equiv}C{-}C{\equiv}C{-}C{\equiv}\{Fe\}]^{2+}$ structure seems reasonable (see Figure 1), as in this mesomeric form of the $C_4$ bridge both metal centers attain a 18-electron configuration.

The $C_4$ bridge of all described compounds gives rise to two signals in the $^{13}$C{$^1$H} NMR, consistent with a centrosymmetric {Fe}−$C_\alpha{\equiv}C_\beta$−


dx.doi.org/10.1021/ja507672g | J. Am. Chem. Soc. 2014, 136, 14560−14569

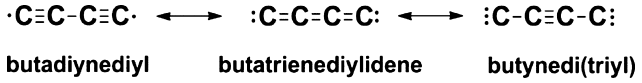


**Figure 1.** Possible mesomeric forms of the $C_4$ bridging ligand.

$C_{\beta'}{\equiv}C_{\alpha'}{-}\{Fe\}$ butadiyne structure and an inversion center located between the $C_\beta$ and $C_\beta'$ of the bridging unit. The signal of the carbon atoms in $\alpha$ position to the iron centers is a quintet for all complexes due to the coupling with the four equatorial P atoms. Also, for centrosymmetric structures with octahedral geometry around the Fe(II) centers and with the electron-rich phosphine ligands arranged equatorially, we expected a singlet in the $^{31}P\{^1H\}$NMR, which was indeed found for all complexes. All complexes are expected to have a local $D_{\infty h}$ symmetry of the $\{Fe\}{-}C{\equiv}C{-}C{\equiv}C{-}\{Fe\}$ arrangement and due to this the complexes are anticipated to give rise to one IR active $\nu_{as}(C_4)$ band. This band is found to possess a prominent and well-distinguishable feature in all IR spectra (Figures S29 − S38). As for **4**−**11** the structure of the central $\{Fe\}C_4\{Fe\}$ motif remains constant, changes of the stretching frequencies of this band can be attributed to the different donor/acceptor properties of the terminal anchor groups *trans* to the bridging ligand (Table 1).

Within the homologous series of compounds, the $\nu_{as}(C_4)$ IR band shifts only slightly. For **4**−**11**, the lowest value of 1936 $cm^{-1}$ is found for the $C_2SnMe_3$ capped compound **5** and the highest value of 1956 $cm^{-1}$ for the dinitro derivative **11**. For the $\nu_s(C_4)$ Raman band, the lowest value of 2086 $cm^{-1}$ is again found for the $C_2SnMe_3$ capped compound **5**, yet the by far highest values of 2103 and 2102 $cm^{-1}$ stem from the vibrational bands of the CN and $C_4SnMe_3$ capped complexes **9** and **6**. A possible explanation for these at first glance unexpected values could be a vibrational coupling between the $\nu_s(C_4)$ band of the bridging ligand and the respective vibrations of the terminal ligands, putting the high-energy band to higher energies and the low-energy band to lower energies.

**X-ray Structure Analyses.** Single crystals were grown of all compounds and allowed a structural characterization using X-ray diffraction studies. The crystal structures of **1** and **6** are discussed elsewhere.[34] Figure 2 depicts the molecular structures of **5** and **7**−**9**, the structures of **2** and **3** are given in Figure S39, and the ones of **4**, **10**, and **11** are in Figure S40. For all complexes discussed here, the bond between the Fe and the $C_\alpha$ of the bridging ligand lies between the values of 1.900(3) Å for **10** and 1.935(5) Å for **5**, which is consistent with a Fe−C single bond. The $C_\alpha{-}C_\beta$ bonds are between 1.215(8) Å for **8** and 1.225(3) Å for **11** and thus still fall into the range of C≡C triple bond separations, whereas the $C_\beta{-}C_\beta'$ bond lengths with values between 1.373(8) Å for **7** and 1.390(7) Å for **10** are slightly shorter than expected for a C(sp)−C(sp) single bond. The Fe−Fe distances are between 7.6117(8) Å for **10** and 7.701(1) Å for **5** and are thus in good accord with the values reported for other terminally open dinuclear compounds, with the $\{Fe(depe)_2\}C_4\{Fe(depe)_2\}$ motif,[34] and are also in range of stopper-type $C_4$ bridged iron dinuclears, such as $[CpFe(dppe)](\mu\text{-}C_4)$[81] and $[(\eta^5\text{-}C_5Me_5)(CO)_2Fe_2](\mu\text{-}C_4)$,[82] which have nonbonding Fe···Fe distances of 7.564 and 7.653 Å, respectively. The values document a butadiynediyl character of the bridging $C_4$ unit, albeit with participation of a butatrienediylidene mesomeric form (Figure 1).

For both complexes **4** and **5** the terminal $C_2$ unit displays bond lengths which correspond to an acetylide structure, i.e., the length of the Fe−C bonds is consistent with a single bond (1.935(5) Å and 1.926(5) Å for **5**, 1.926(2) Å for **4**), and the C−C bonds are in the range expected for triple bonds (1.220(5) Å, and 1.210(8) Å for **5**, 1.207(4) Å for **4**). For all molecules, the ligand geometry around the Fe cores is pseudo octahedral, with the four P atoms occupying equatorial positions, whereas the end group is lying on an axial position *trans* to the bridging ligand. The average Fe−P distance of the neutral compounds lies between 2.220 Å for the $C_2SnMe_3$ capped compound **5** and 2.248 Å for the $NO_2$ terminated **11**. The average Fe−P distance of the dicationic compounds **2** and **3** (2.252 and 2.271 Å, respectively) is slightly elongated compared to the neutral compounds, yet all values lie in the range of $\{Fe(depe)_2\}$ centers reported earlier. The comparably long Fe−P distance of **3** apparently causes a high-field shift of the signal in the $^{31}P\{^1H\}$ spectrum as described above.

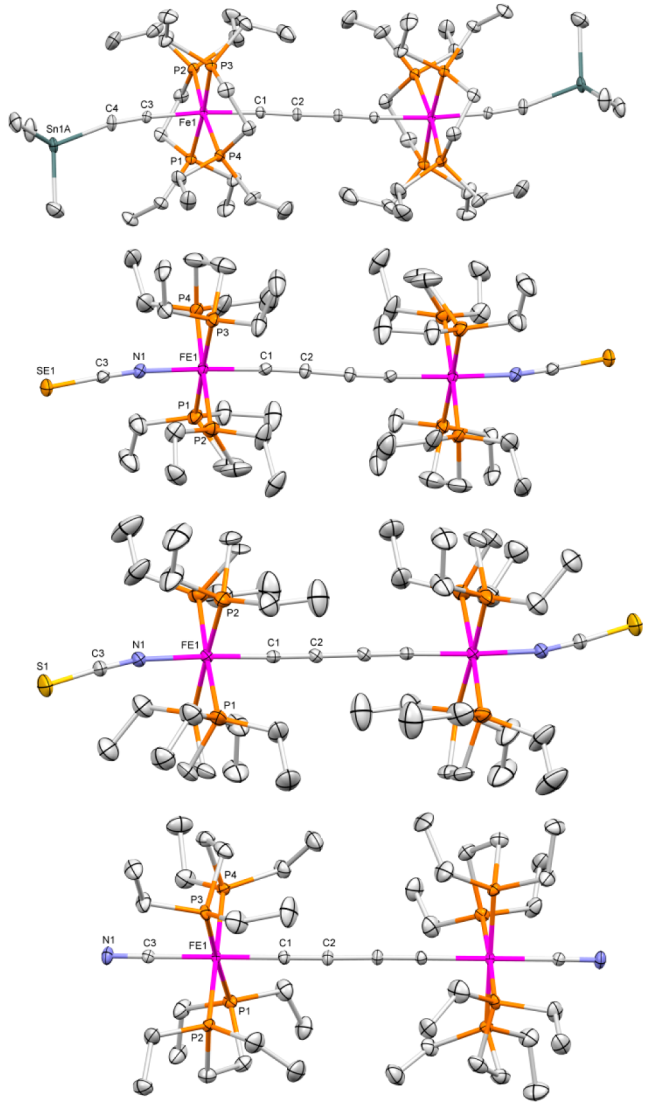


**Figure 2.** Molecular structures of **5** and **7**−**9** (from top to bottom). Ellipsoids are set at 30% probability level. Solvent molecules and selected hydrogen atoms are omitted for clarity. See Table S2 for selected bond lengths, distances, and angles.

The *cisoid* (bow-shaped) and *transoid* (S-shaped) distortions, which are a common phenomenon for $C_n$ (with $n \geq 4$) bridged dinuclear $\{M\}C_n\{M\}$ compounds, are unincisive for the structures discussed here. Compounds **4**, **9**, and **11** show minor *cisoid* distortions along the metal−$C_4$−metal backbone, yet the Fe−$C_\alpha$−$C_\beta$ angle, which makes the largest contribution to this distortion, lies in the range of 175.9(3)−176.7(2)° (Table S2) and is almost linear. Compounds $[\mathbf{2}]^{2+}$, $[\mathbf{3}]^{2+}$, **5** and **7**−**10** could be described as *transoid* distorted, yet this distortion is only distinct for the thiol capped compound **9**, where the Fe−$C_\alpha$−$C_\beta$ angle is 173.4(3)°. Gladysz et al. showed via DFT calculations that the energetic barrier for *cisoid* distortions for $\{M\}C_n\{M\}$ fragments is quite small[83] and also noted the tendency that distortions from linearity are often located at the end of the linear chain.[84] When the lengths of the terminal ligands are taken into account, this tendency can indeed be observed for the presented molecules, in particular for terminal groups consisting of three or more atoms, which are linearly arranged, i.e., complexes **5**−**8** and, albeit to a lesser extent, the $C_2H$ capped **4**. Interestingly, the distortion of the linearity is emanating from the iron center for compounds **7** and **8** illustrated by a Fe−N−C bond angle deviating considerably from linearity (172.9(4) and 169.4(5)° for


dx.doi.org/10.1021/ja507672g | J. Am. Chem. Soc. 2014, 136, 14560−14569

NCSe **7** and NCS **8**, respectively). For **4** and **5** the distortion is located completely on the terminal ligand, with the C−C−Sn angles of **5** at 162.9(5)° and 158.0(5)°. However, these values cannot considered with confidence because of the disorder observed on the terminal ligands. For both **7** and **8**, the Fe−N−C bond angle was expected to be <180° due to the lone electron pair on the N nuclei but instead found to be close to 180° ($\angle_{(C3-N1-Fe1)}$ = 177.6(4)° for **7** and 176.2(6)° for **8**, Table S2).

The comparably short N−C bond (1.161(6)Å for **7** and 1.135(7) Å for **8**, Table S2) suggests a considerable influence of the $M-N^{+}\equiv C-Se^{-}$ and $M-N^{+}\equiv C-S^{-}$ canonical structures.[85] Neither of the terminal ligands chosen for this project nor the depe ligands are sterically excessively demanding. Consequently it can be reasoned that the observed deviations from linearity stem from intermolecular interactions and crystal packing effects.[84,86]

**Cyclic Voltammetry.** Cyclic voltammetry experiments were carried out to probe the thermodynamic stability of the reported complexes in all accessible oxidation states. Compounds **4**, **6**, **8**, **9**, and **11** exhibit three and complexes **5** and **7** two well-defined and reversible oxidation waves, while for **10** no reversible process was found (Table 2 and Supporting Information).

**Table 2. Cyclic Voltammetry Data of the Complexes 4−11[a]**

| compd. | $E_{1/2}$ (0/+1) [mV] | $E_{1/2}$ (+1/+2) [mV] | $\Delta E$ [mV] | $K_c$ | $E_{1/2}$ (+2/+3) [mV] |
|---|---|---|---|---|---|
| **4** | −453 | 10 | 462 | $7.7 \times 10^7$ | 799 |
| **5** | −458 | 5 | 463 | $7.9 \times 10^7$ | – |
| **6** | −503 | −48 | 456 | $6.0 \times 10^7$ | 671 |
| **7** | −428 | 24 | 452 | $5.1 \times 10^7$ | – |
| **8** | −372 | 106 | 478 | $14.5 \times 10^7$ | 848 |
| **9** | −421 | 10 | 431 | $2.2 \times 10^7$ | 729 |
| **10** | – | – | – | – | – |
| **11** | −497 | −14 | 483 | $17.7 \times 10^7$ | 735 |

[a]Measurements at 300 K in THF/$Bu_4NPF_6$ (0.1M) with an Au working electrode, a Pt counter electrode, and an Ag reference electrode. *E* vs $Fc^{0/+}$ (external).

Two oxidation waves are associated with the consecutive oxidation of the two metal centers, whereas the third one, positioned at a significantly more positive potential, is associated with the oxidation of the bridging ligand.[34,37] The existence of two metal-based oxidations for a highly symmetric molecule possessing a formal inversion center in the middle of the bridging ligand is a strong indicator for high charge delocalization over the length of the rigid-rod molecule,[23] which demonstrates that the butadiyne bridging ligand is actively supporting charge transport between the redox-active iron centers.[87]

The thiol-capped compound **10** does not exhibit any reversible oxidation process in the THF/$Bu_4NPF_6$ electrolyte, an electrochemical behavior which would be consistent with the oxidative formation of dithio species. This explanation is also in agreement with the observed disposition of **10** to decompose in solution and deposit as a thin film on the electrodes during the cyclic voltammetry experiments. The $C_2SnMe_3$ capped **5** and the NCSe capped **7** both only show two reversible oxidation waves, both in a range associated with metal-based oxidations (Figure S47 for **7** and S44 for **5**). For **5**, the absence of a third reversible oxidation wave is interesting as the structurally highly similar $C_2H$ capped **4** shows the carbon based oxidation. When recording cyclic voltammograms of **5** with a broader electrochemical window (Figure S43), one can observe that, while there is no reversible third oxidation wave, the first two oxidations are still present and furthermore still reversible. This indicates that processes linked to a cleavage of the trimethylstannyl group in the higher potential range might be responsible for the absence of a carbon based oxidation. For the NCSe capped complex **7** all three oxidations are observable, but the re-reduction processes are not reversible (Figure S46). Upon narrowing the potential window, two fully reversible oxidation waves were detected (Figure S47). This behavior could be interpreted in terms of insolubility of the 3-fold oxidized species in the electrolyte. Except for the thiol-capped complex **10** the mixed valence forms show very good thermodynamic stabilization as derived from the high $K_c$ values in the range of $10^7$ (Table 2).[23]

Based on the $MC_4M$ in common motif molecules, **4**−**11** show high structural uniformity. Nonetheless, number and position of the oxidation waves as well as the peak separation evidence a noticeable variance (Table 2). Peak separation and $K_c$ values depend on the distance between the metal centers,[88] the electron density at the metal centers, electrostatic interactions, solvation, ion pairing with the electrolyte, and structural distortions.[23] For the complexes reported here, the differences in the nonbonding Fe···Fe distances (see Table 3) are small and can only partially explain the variance. The $\Delta E$ values are expected to increase with the electron density of the metal center, yet, similar to the IR and Raman data, the interpretation based on the electron-donating and -accepting properties of the terminal anchoring ligand is however not fully conclusive. Still, the cyclic voltammetry data corroborate that by changing one structural motif in an otherwise homologous series of organometallic wire-type molecules allows modification of their physical, spectroscopic, and electronic properties.

**Table 3. Selected Distances (Å) Computed at the According to the HSAB Principle (ref 49)[a]**

| X | X···X (X-ray) (Å) | X···X (DFT)[c] (Å) | LUMO (eV) | HOMO (eV) | $\Delta E_{(H-L)}$ (eV) | $\chi$ (eV) |
|---|---|---|---|---|---|---|
| SH | S···S = 12.3435(17) | 12.54 | −0.33 | −4.16 | 3.83 | 2.25 |
| $NO_2$ | O···O = 12.830(3) | 13.15 | −0.57 | −4.58 | 4.01 | 2.58 |
| CN | N···N = 13.738(4) | 13.93 | −0.39 | −4.41 | 4.02 | 2.40 |
| $C_2H$ | C···C = 13.896(6) | 14.08 | −0.28 | −4.07 | 3.79 | 2.18 |
| NCS | S···S = 16.940(3) | 17.34 | −0.57 | −4.60 | 4.03 | 2.59 |
| NCSe | Se···Se = 17.3280(15) | 17.59 | −0.60 | −4.62 | 4.02 | 2.61 |
| $C_4H$ | C···C = 19.015(12)[b] | 19.26 | −0.40 | −4.33 | 3.93 | 2.37 |

[a]An increase of the HOMO/LUMO gap is PBE1PBE/LANL2DZ level and derived from X-ray studies, HOMO and LUMO energies (eV), HOMO/LUMO gap (eV), and absolute electronegativity $\chi$ computed at the PBE1PBE/LANL2DZ//PBE1PBE/6-311+g(d) level. [b]See ref 34. [c]See Computational Details section.

## DFT CALCULATIONS

The molecular geometries of the model complexes **4**-Me, $\mathbf{6}_H$-Me, **7**-Me, **8**-Me, **9**-Me, **10**-Me, and **11**-Me were optimized with the Gaussian 03 program package[66] using the hybrid functional PBE1PBE[67] in conjunction with the LanL2DZ basis set.[67−70] Geometries were optimized with a $C_i$ (inversion center) or a $C_2$ (2-fold axis) symmetry, and the ethyl groups of the depe ligands were replaced by methyl groups (dmpe = 1,2-bis-(dimethylphosphino)ethane). As the $SnMe_3$ groups of **5** and **6** are expected to cleave off to form a covalent C−Au bond, calculations were carried out for the H terminated models **4**-Me ($HC\equiv C(dmpe)_2Fe-C_4-Fe(dmpe)_2C\equiv CH$) and $\mathbf{6}_H$-Me ($HC_4(dmpe)_2Fe-C_4-Fe(dmpe)_2C_4H$).

The computed distances for the model complexes compare well with the structural data derived from the X-ray studies (Tables 3 and S2). In all cases, the computed distances are slightly elongated, which is attributed to intermolecular interactions and packing effects within the crystal structures.[84,89] The deviation is highest for the $NO_2$ terminated complexes **11** and **11**-Me, where the computed O···O′ distance of 13.15 Å is


dx.doi.org/10.1021/ja507672g | J. Am. Chem. Soc. 2014, 136, 14560−14569

longer by about 2.5% compared to the distance of 12.83 Å found in the X-ray experiment. Single-point calculations were carried out with the PBE1PBE functional and the 6-311+G(d) basis set for the determination of the molecular orbital energies. The HOMO and LUMO energies are given in Table 3 and in Figure S51 arranged in the order of the increasing molecular length. The absolute energies of the HOMO lie between −4.62 eV for **7**-Me and −4.07 eV for **4**-Me, and the ones of the LUMO are between −0.60 eV for **7**-Me and −0.28 eV for **4**-*Me*. To achieve a resonant transport, the molecular orbitals of the probed molecule should be aligned to $E_F$ of the macroscopic electronic leads. As expected for 18-electron metal complexes, the HOMO/LUMO gap $\Delta E_{(H-L)}$ is relatively large and lies between 3.79 eV for **4**-Me and 4.03 eV for **8**-Me. The work of Pearson established that $\Delta E_{(H-L)}$ derived from DFT calculations can be correlated to hardness associated with a weakening of polarizability and therefore an increase in chemical hardness. For the discussed molecules, the hardness is consequently increasing in the order **4**-Me < **10**-Me < $\mathbf{6}_H$-Me < **11**-Me < **9**-Me = **7**-Me < **8**-Me, whereas for the electronegativity $\chi$ the opposite trend is followed (Table 3 and Figure S51).

The Fermi energy of the Au electrodes is reasonably close to the energetic range of the HOMO's of all complexes discussed here. Assuming no charge transfer and MO broadening upon coupling the compounds to leads and taking the calculated HOMO levels of the isolated compounds as a measure for the resonant transport conditions, their alignment to and interaction with $E_F$ would be in the order **8**-Me < **9**-Me = **7**-Me < **11**-*Me* < $\mathbf{6}_H$-Me. It has to be noted, however, that the calculations were carried out for isolated molecules in the gas phase, whereas for the MCBJ experiments, a solid-state behavior of the complexes has to be assumed. The interactions with the Au electrodes, such as charge transfer, hybridization, and broadening of MO due to coupling, which are especially for the understanding of the covalently bonded **Au−5′−Au** and **Au−6′−Au** junctions, are not considered by the chosen level of DFT.

A more detailed computational study of the $C_4SnMe_3$, $C_2SnMe_3$, NCS, NCSe, and CN terminated molecules and their conductance behavior under bias, taking the interactions with the Au electrodes into account, is reported elsewhere.[90]

Still, the calculations show that the energetic positions of the molecular orbitals and the extent of the HOMO/LUMO gap can be tuned by varying the terminal ligand of a X{M}$C_4${M}X, even if metal center, bridging, and equatorial ligands are kept unaltered.

**Single-Molecule Transport Measurements.** Based on the results of the spectroscopic and electrochemical studies as well as of the computational findings, the coordinatively binding complexes **7**−**9** and the $SnMe_3$ capped compounds **5** and **6** were chosen for transport measurements at the single-molecule level using a mechanically controllable break-junction. The results are summarized in Figure 3 and Table 4. As the direct electron tunneling between the Au electrodes is an non-negligible conductance channel in a molecular transport junction,[46] the electrode spacing of the corresponding metal−molecule−metal system has to be taken into account. The junction **Au−5′−Au** formed after the cleavage of the $SnMe_3$ group has a resulting junction length ($C_\beta$−$C_\beta$ distance of 13.95 Å after cleavage) comparable to **Au−9−Au** (with a N−N distance of 13.74 Å), whereas the **Au−6′−Au** junction ($C_\beta$-$C_\beta$ distance of 19.02 Å after cleavage) is in a length range with the NCS (S−S distance of 16.94 Å) and NCSe (Se−Se distance of 17.33 Å) junctions **Au−8−Au** and **Au−7−Au**.

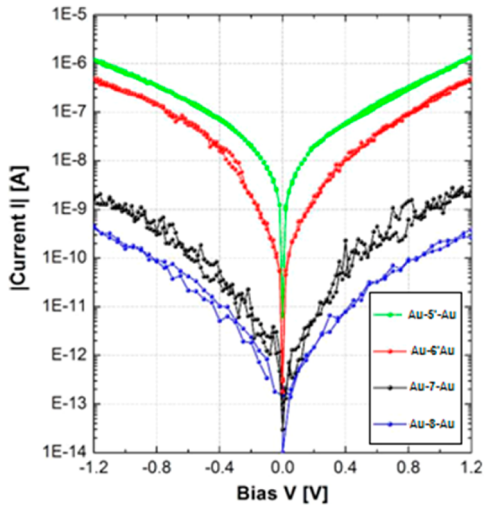


**Figure 3.** Current−voltage ($I$−$V$) characteristics taken at 300 K for the junctions **Au−5′−Au** (green), **Au−6′−Au** (red), **Au−7−Au** (black), and **Au−8−Au** (blue).

**Table 4. Typical Current Values for 5′, 6′, 7, and 8 Averaged From the $I$−$V$ Double Sweeps at 200 mV and at 1 V**

| | current level [A] extracted at different bias | |
|---|---|---|
| compd. | 200 mV | 1 V |
| **5′** | $2.03 \times 10^{-8}$ | $6.51 \times 10^{-7}$ |
| **6′** | $5.56 \times 10^{-9}$ | $2.13 \times 10^{-7}$ |
| **7** | $6.66 \times 10^{-12}$ | $1.29 \times 10^{-9}$ |
| **8** | $1.79 \times 10^{-12}$ | $1.77 \times 10^{-10}$ |

For the $C_2$ and $C_4$ terminal substituents of the **Au−5′−Au** and **Au−6′−Au** junctions, acetylenic-, vinylidenic-, and (alkynyl vinylidenic)-configured bonding schemes can be postulated upon binding to the Au electrodes. A computational study of the possible bonding motifs of the $C_4SnMe_3$ terminated molecule suggested that the different bonding schemes do not differ significantly in their conductance behavior.[90] To elucidate the bonding schemes of the $C_2$ and $C_4$ anchor groups, further spectroscopic experiments are planned, e.g., XPS and Raman spectroscopy.

For **9**, only histograms have been acquired revealing a less pronounced accumulation at $8.1 \times 10^{-7}$ $G_0$, most likely due to unstable binding situations as the phosphine ligands sterically hinder the short CN anchor to bind to the Au surface. The low conductance and the sterical hindrance renders the CN end group rather inefficient for electron injection. In contrast to **9**, the statistical transport measurements of **5′**, **6′**, **7**, and **8** provided reproducible and consistent results that are displayed in Figure 3. The data presented show representative and individual four-step (from 0.0 to −1.2 to 0.0 V and from 0.0 to +1.2 and 0.0 V) $I$−$V$ characteristics for **Au−5′** (green), **6′** (red), **7** (black), and **8** (blue) acquired at room temperature and extracted from large statistical data sets of more than 1000 $I$−$V$ characteristics.[74,90] On the first glance, the $I$−$V$ characteristics at 300 K look similar regarding their functional behavior and differ strongly in: (A) the current amplitude at both low and high bias, (B) the current onset (at zero bias), and (C) the signal-to-noise ratio. These parameters differ for the four end groups because of the following reasons: At 300 K, a finite local density of states (LDOS) is arising at $E_{F,Au}$ from the energy level of the MOs being broadened thermally and by coupling the MO to leads.[91]


dx.doi.org/10.1021/ja507672g | J. Am. Chem. Soc. 2014, 136, 14560−14569

Additionally, $E_F$ is broadened at 300 K giving rise to a finite conductance and hence a finite current at zero bias. In Figure 3, the current is generally increasing with increasing bias for all compounds, indicating that the frontier MOs get energetically better aligned with the chemical potentials of left or right leads. In contrast to measurements taken at low temperatures (<100 K), where resonant transport properties are being revealed by distinct steps in the $I-V$ curves,[92] at 300 K the MOs are smeared out, and generally a nonlinear (almost exponential) functional $I-V$ behavior with only a few distinguishable features is found.

We will discuss in the following the two comparative parameters current level and current increase and further quantify the current fluctuations as measure for the junction's high-field stability:

(A) The current levels of compound **8** (blue; $(1.5-2.2) \times 10^{-10}$ A at $\pm 1.0$ V) and **7** (black; $(1.0-1.8) \times 10^{-9}$ A at $\pm 1.0$ V) differ by almost 1 order of magnitude, rendering NCS coupling the weakest among all coupling motifs studied here. Compounds **5′** and **6′** with direct C−Au coupling reveal current levels ranging between $(6.0-7.2) \times 10^{-7}$ and $(2.0-2.4) \times 10^{-7}$ A at $\pm 1.0$ V, an approximately 100- and a 1000-fold increase in current compared to −NCSe and −NCS termination. As the Fe−$C_4$−Fe molecular backbone is kept equal in all four compounds, charging effects that may shift the MO's energy levels in Au−molecule−Au systems significantly compared to the isolated molecules are expected to be similar for all compounds. Hence, the current levels represent in a first-order approximation the electronic coupling strength of the corresponding end group. Consequently the NCSe termination provides a better coupling compared to NCS as the current is increased by a factor of 10. The direct C−Au bond, as established during cleavage of the $SnMe_3$ group, reveals an at least 2 orders of magnitude higher current level compared to NCSe (**7**) and 3 orders of magnitude compared to the NCS (**8**) termination. This relative increase in the transport characteristics is in agreement with findings on the low-bias conductance of S−Au and C−Au coupled oligophenylenes[47] as well as DFT calculations[90] that indicate a strong electronic hybridization between molecular and metal states.

(B) The functional current increase when starting the bias sweep at zero is similar for NCS and NCSe termination, in contrast to a very abrupt increase in current for the direct C−Au coupling. In the latter case, the current increases, e.g., from 0.4 pA to 0.4 nA (**4**) or 1.0 nA (**5′**) within only 20 mV. This indicates that resonant MOs or MOs close-to-resonance are available at $E_F$, presumably established by spatial overlap of molecular and metal states leading to electronic hybridization[90] as discussed above. Additional to the zero-bias current level, the slopes of the $I-V$ curves differ. They are found to behave almost linear on the semilog representation at biases larger than approximately $\pm 0.3$ V for **5′** and larger than $\pm 0.4$ V for **6′**, respectively. This indicates that for the C−Au coupling, the contribution of the MOs next to the frontier ones to transport is minor in the bias window available. From the DFT calculations, it seems that the "conducting" orbitals in the molecule−metal interface are assumed to be of $\pi$ type as they constitute the HOMO/LUMO region and are therefore more suited for electron transport.

(C) The last comparative parameter concerns the noise in the current as a measure for the junction stability under electrical load. Despite of the 3 orders of magnitude higher current, the current fluctuations are 1 order of magnitude smaller for C−Au coupling compared with NCS coupling, in particular for voltages larger than $\pm 0.4$ V (Figure S52).

This indicates that even under large current densities, the C−Au bond has very limited bond fluctuations and that the electron−phonon-coupling in the Fe−$C_4$−Fe backbone is rather small in all compounds.

We summarize from the transport properties of **5′**, **6′**, **7**, and **8** as displayed in Figure 3 and Table 4 that variations of the anchoring motif strongly and directly influence the transport properties of the corresponding Au−molecule−Au system. A strong increase in conductance occurs in particular when employing covalent C−Au bonds. The end group therefore enables to tune the transport properties over more than 3 orders of magnitude.

## CONCLUSION

It was demonstrated that the class of {Fe}−C≡C−C≡C−{Fe} ({Fe} = $Fe(depe)_2$, depe = 1,2-bis(diethylphospino)ethane) organometallic complexes can be modified to incorporate terminal substituents capable of binding to Au electrodes to form stable single-molecular junctions by establishing either covalent or coordinative bonds to Au electrodes. A triad of precursor molecules with highly reactive ligands in *trans* position to the bridging butadiyne was designed to target this terminal substituent function. Synthetic strategies were developed to introduce CN, SH and $NO_2$, $C_2H$, $C_2SnMe_3$, $C_4SnMe_3$, NCSe, and NCS substituents at the terminal sites.

The molecular design of the precursor molecules as well as the strategy for the synthetic pathways enable a facile modification of the termini of the X{Fe}−C≡C−C≡C−{Fe}X system to tailor the molecule−metal coupling for specific applications.

The systematic synthetic approach allows a variation of the structural motifs, involving the metal centers, the bridging ligand, and the equatorial ligand sphere, to be modified in order to modulate the charge transport properties. The end groups chosen are conjugated moieties and covalently bound to the Fe centers. Various binding motifs to Au electrodes were tested that form coordinative to covalent bonds, enabling to electronically extend the electron delocalization of the {Fe}−C≡C−C≡C−{Fe} core toward the leads by hybridization of MO and metal states as it takes place upon a covalent C−Au binding. The C−Au end groups allow a direct charge injection into the redox active molecules. The utilization of the sp-hybridized and electronically highly versatile butadiyne bridging ligand was demonstrated to drastically increase charge transport rates by lowering the injection barrier across the molecule−metal interface. DFT model studies suggest that the HOMO/LUMO gap can be tuned by varying the X groups of a X{M}$C_4${M}X system even if the metal centers and bridging and equatorial ligands are kept unaltered.

To allow a comparison of the current levels, molecules with comparable overall molecular lengths were chosen for single-molecule transport measurements at 300 K under ultrahigh vacuum conditions. For the $C_2$ terminated **5′** a current level of approximately $6.5 \times 10^{-7}$ A at 1.0 V was achieved, reaching 1% of the maximal current available for Au−Au quantum point


dx.doi.org/10.1021/ja507672g | J. Am. Chem. Soc. 2014, 136, 14560−14569

contacts ($77.6 \times 10^{-6}$ A at 1.0 V assuming one conductance channel). Additionally, both C−Au bonded systems exhibited a higher stability and less fluctuations in the transport properties. When comparing the conductance of the organometallic compounds as a function of wire length, the Fe-based molecules **5′** and **6′** outperform the currently best conductive molecular wire systems (at comparable length), the poly-*p*-phenylene possessing a C−Au coupling.[47] The covalently bonded $C_2$ and $C_4$ molecular junctions behave like highly conjugated systems.

Therefore, the utilization of covalent C(sp)−Au bonds and of strongly electronically delocalized polycarbyl chains with embedded metal centers into the molecular backbone is an attractive concept to achieve low-ohmic molecular wires generating hybridized metal−molecule interfaces, close MO level alignments with $E_F$ and electron pathways delocalized across the backbone. These three parameters provide high-conductive molecular wires that are strongly required for future nanoelectronics.

## ■ ASSOCIATED CONTENT

### Supporting Information

Experimental details describing the syntheses as well as giving details of the NMR spectroscopy (Figures S1−S28, Table S1), IR spectroscopy (Figures S29−S38), cyclic voltammetry (Figures S42−S50) experiments, refinement details and crystallographic data (Tables S2−S5, Figures S39−S41 and CIFs) for the X-ray diffraction studies, computational results (Figure S51, and a XYZ file with the Cartesian coordinates of all optimized geometries) and additional transport results (Figure S52). This material is available free of charge via the Internet at http://pubs.acs.org.

## ■ AUTHOR INFORMATION


### Corresponding Authors

hberke@chem.uzh.ch
venkatesan.koushik@chem.uzh.ch
eml@zurich.ibm.com


### Notes

The authors declare no competing financial interest.

## ■ ACKNOWLEDGMENTS

Funding from the National Research Program "Smart Materials" (NRP 62, grant 406240-126142) of the Swiss National Science Foundation (SNSF) and the University of Zürich is gratefully acknowledged. We thank T. Fox for his help with the NMR studies. We acknowledge the technical support of U. Drechsler, M. Tschudy, and Ch. Rettner and the scientific discussions with R. Stadler, G. Kastlunger, M. Koch, N. Mosso, and G. Puebla-Hellmann.

## ■ REFERENCES


(1) Carroll, R. L.; Gorman, C. B. *Angew. Chem., Int. Ed.* **2002**, No. 41, 4378−4400.
(2) Lörtscher, E.; Ciszek, J. W.; Tour, J.; Riel, H. *Small* **2006**, *2* (8−9), 973−977.
(3) Reed, M. A. *Science* **1997**, *278* (5336), 252−254.
(4) Aviram, A.; Ratner, M. A. *Chem. Phys. Lett.* **1974**, *29* (2), 277−283.
(5) Tour, J. M. *Acc. Chem. Res.* **2000**, *33* (11), 791−804.
(6) Cuniberti, G. *Introducing molecular electronics*; Springer: Berlin, 2005.
(7) Kaliginedi, V.; Moreno-García, P.; Valkenier, H.; Hong, W.; García-Suárez, V. M.; Buiter, P.; Otten, J. L. H.; Hummelen, J. C.; Lambert, C. J.; Wandlowski, T. *J. Am. Chem. Soc.* **2012**, *134* (11), 5262−5275.
(8) Wen, H.-M.; Yang, Y.; Zhou, X.-S.; Liu, J.-Y.; Zhang, D.-B.; Chen, Z.-B.; Wang, J.-Y.; Chen, Z.-N.; Tian, Z.-Q. *Chem. Sci.* **2013**, *4* (6), 2471.
(9) Hong, W.; Manrique, D. Z.; Moreno-García, P.; Gulcur, M.; Mishchenko, A.; Lambert, C. J.; Bryce, M. R.; Wandlowski, T. *J. Am. Chem. Soc.* **2012**, *134* (4), 2292−2304.
(10) Chen, F.; Hihath, J.; Huang, Z.; Li, X.; Tao, N. J. *Annu. Rev. Phys. Chem.* **2007**, *58* (1), 535−564.
(11) Zotti, L. A.; Kirchner, T.; Cuevas, J.-C.; Pauly, F.; Huhn, T.; Scheer, E.; Erbe, A. *Small* **2010**, *6* (14), 1529−1535.
(12) Luo, L.; Choi, S. H.; Frisbie, C. D. *Chem. Mater.* **2011**, *23* (3), 631−645.
(13) Lu, Q.; Liu, K.; Zhang, H.; Du, Z.; Wang, X.; Wang, F. *ACS Nano* **2009**, *v3* (12), 3861−3868.
(14) He, J.; Chen, F.; Li, J.; Sankey, O. F.; Terazono, Y.; Herrero, C.; Gust, D.; Moore, T. A.; Moore, A. L.; Lindsay, S. M. *J. Am. Chem. Soc.* **2005**, *127* (5), 1384−1385.
(15) Ho Choi, S.; Kim, B.; Frisbie, C. D. *Science* **2008**, *320* (5882), 1482−1486.
(16) Zhao, X.; Huang, C.; Gulcur, M.; Batsanov, A. S.; Baghernejad, M.; Hong, W.; Bryce, M. R.; Wandlowski, T. *Chem. Mater.* **2013**, *25* (21), 4340−4347.
(17) Prins, F.; Monrabal-Capilla, M.; Osorio, E. A.; Coronado, E.; van der Zant, Herre S. J. *Adv. Mater.* **2011**, *23* (13), 1545−1549.
(18) Low, P. J. *Dalton Trans.* **2005**, No. 17, 2821.
(19) Wuttke, E.; Hervault, Y.-M.; Polit, W.; Linseis, M.; Erler, P.; Rigaut, S.; Winter, R. F. *Organometallics* **2014**, *33*, 4672−4686.
(20) O'Hanlon, D. C.; Cohen, B. W.; Moravec, D. B.; Dallinger, R. F.; Hopkins, M. D. *J. Am. Chem. Soc.* **2014**, *136*, 3127−3136.
(21) Creutz, C.; Taube, H. *J. Am. Chem. Soc.* **1973**, *95* (4), 1086−1094.
(22) Tuccitto, N.; Ferri, V.; Cavazzini, M.; Quici, S.; Zhavnerko, G.; Licciardello, A.; Rampi, M. A. *Nat. Mater.* **2008**, *8* (1), 41−46.
(23) Aguirre-Etcheverry, P.; O'Hare, D. *Chem. Rev.* **2010**, *110* (8), 4839−4864.
(24) Costuas, K.; Rigaut, S. *Dalton Trans.* **2011**, *40* (21), 5643.
(25) Low, P. J. *Coord. Chem. Rev.* **2013**, *257* (9−10), 1507−1532.
(26) Szafert, S.; Paul, F.; Meyer, W. E.; Gladysz, J. A.; Lapinte, C. *C. R. Chim.* **2008**, *11* (6−7), 693−701.
(27) Bruce, M. I.; Costuas, K.; Davin, T.; Ellis, B. G.; Halet, J.-F.; Lapinte, C.; Low, P. J.; Smith, M. E.; Skelton, B. W.; Toupet, L.; White, A. H. *Organometallics* **2005**, *24* (16), 3864−3881.
(28) Montigny, F. de; Argouarch, G.; Costuas, K.; Halet, J.-F.; Roisnel, T.; Toupet, L.; Lapinte, C. *Organometallics* **2005**, *24* (19), 4558−4572.
(29) Lissel, F.; Blacque, O.; Venkatesan, K.; Berke, H. *Organometallics* **2014**, submitted.
(30) Haines, D. E.; O'Hanlon, D. C.; Manna, J.; Jones, M. K.; Shaner, S. E.; Sun, J.; Hopkins, M. D. *Inorg. Chem.* **2013**, *52* (16), 9650−9658.
(31) Low, P. J.; Bock, S. *Electrochim. Acta* **2013**, *110*, 681−692.
(32) Pevny, F.; Di Piazza, E.; Norel, L.; Drescher, M.; Winter, R. F.; Rigaut, S. *Organometallics* **2010**, *29* (22), 5912−5918.
(33) Wuttke, E.; Pevny, F.; Hervault, Y.-M.; Norel, L.; Drescher, M.; Winter, R. F.; Rigaut, S. *Inorg. Chem.* **2012**, *51* (3), 1902−1915.
(34) Lissel, F.; Fox, T.; Blacque, O.; Polit, W.; Winter, R. F.; Venkatesan, K.; Berke, H. *J. Am. Chem. Soc.* **2013**, *135* (10), 4051−4060.
(35) Ward, M. D. *Chem. Soc. Rev.* **1995**, *24* (2), 121.
(36) Frohnapfel, D. S.; Woodworth, B. E.; Thorp, H. H.; Templeton, J. L. *J. Phys. Chem. A* **1998**, *102* (28), 5665−5669.
(37) Guillemot, M.; Toupet, L.; Lapinte, C. *Organometallics* **1998**, *17* (10), 1928−1930.
(38) Paul, F.; Lapinte, C. *Coord. Chem. Rev.* **1998**, *178−180, Part 1* (0), 431−509.
(39) Halet, J.-F.; Lapinte, C. *Coord. Chem. Rev.* **2013**, *257* (9−10), 1584−1613.
(40) Quardokus, R. C.; Lu, Y.; Wasio, N. A.; Lent, C. S.; Justaud, F.; Lapinte, C.; Kandel, S. A. *J. Am. Chem. Soc.* **2012**, *134* (3), 1710−1714.

(41) Marques-Gonzalez, S.; Yufit, D. S.; Howard, Judith A. K.; Martin, S.; Osorio, H. M.; Garcia-Suarez, V. M.; Nichols, R. J.; Higgins, S. J.; Cea, P.; Low, P. J. *Dalton Trans.* **2013**, *42* (2), 338−341.
(42) Mayor, M.; Hänisch, C. von; Weber, H. B.; Reichert, J.; Beckmann, D. *Angew. Chem., Int. Ed.* **2002**, *41* (7), 1183−1186.
(43) Benameur, A.; Brignou, P.; Di Piazza, E.; Hervault, Y.-M.; Norel, L.; Rigaut, S. *New J. Chem.* **2011**, *35* (10), 2105.
(44) Luo, L.; Benameur, A.; Brignou, P.; Choi, S. H.; Rigaut, S.; Frisbie, C. D. *J. Phys. Chem. C* **2011**, *115* (40), 19955−19961.
(45) Kim, B.-S.; Beebe, J.; Olivier, C.; Rigaut, S.; Touchard, D.; Kushmerick, J.; Zhu, X.-Y.; Frisbie, C. *J. Phys. Chem. C* **2007**, *111* (20), 7521−7526.
(46) Gotsmann, B.; Riel, H.; Lörtscher, E. *Phys. Rev. B* **2011**, *84*, 205408.
(47) Chen, W.; Widawsky, J. R.; Vazquez, H.; Schneebeli, S. T.; Hybertsen, M. S.; Breslow, R.; Venkataraman, L. *J. Am. Chem. Soc.* **2011**, *133* (43), 17160−17163.
(48) Nath, S.; Ghosh, S.; Kundu, S.; Praharaj, S.; Panigrahi, S.; Pal, T. *J. Nanopart. Res.* **2006**, *8* (1), 111−116.
(49) Pearson, R. G. *Chemical hardness*; Wiley-VCH: Weinheim, Germany, 1997.
(50) Mishchenko, A.; Zotti, L. A.; Vonlanthen, D.; Bürkle, M.; Pauly, F.; Cuevas, J. C.; Mayor, M.; Wandlowski, T. *J. Am. Chem. Soc.* **2011**, *133* (2), 184−187.
(51) Lörtscher, E.; Cho, C. J.; Mayor, M.; Tschudy, M.; Rettner, C.; Riel, H. *ChemPhysChem* **2011**, *12* (9), 1677−1682.
(52) Vazquez, H.; Skouta, R.; Schneebeli, S.; Kamenetska, M.; Breslow, R.; Venkataraman, L.; Hybertsen, M. *Nat. Nanotechnol.* **2012**, *7* (10), 663−667.
(53) Reed, M. A. *Science* **1997**, *278* (5336), 252−254.
(54) Sheridan, M. V.; Lam, K.; Geiger, W. E. *J. Am. Chem. Soc.* **2013**, *135* (8), 2939−2942.
(55) Sheridan, M. V.; Lam, K.; Geiger, W. E. *Angew. Chem., Int. Ed.* **2013**, *52* (49), 12897−12900.
(56) Pearson, R. G. *J. Chem. Sci.* **2005**, *117*, 369.
(57) Hong, W.; Li, H.; Liu, S.-X.; Fu, Y.; Li, J.; Kaliginedi, V.; Decurtins, S.; Wandlowski, T. *J. Am. Chem. Soc.* **2012**, *134* (47), 19425−19431.
(58) Cheng, Z.-L.; Skouta, R.; Vazquez, H.; Widawsky, J. R.; Schneebeli, S.; Chen, W.; Hybertsen, M. S.; Breslow, R.; Venkataraman, L. *Nat. Nanotechnol.* **2011**, *6* (6), 353−357.
(59) Ballesteros, L. M.; Martín, S.; Momblona, C.; Marqués-González, S.; López, M. C.; Nichols, R. J.; Low, P. J.; Cea, P. *J. Phys. Chem. C* **2012**, *116* (16), 9142−9150.
(60) *CrysAlis*$^{Pro}$; Agilent Technologies (formerly Oxford Diffraction): Yarnton, England, 2011.
(61) Clark, R. C.; Reid, J. S. *Acta Crystallogr., Sect. A: Found. Crystallogr.* **1995**, *51* (6), 887−897.
(62) Farrugia, L. J. *J. Appl. Crystallogr.* **1999**, *32* (4), 837−838.
(63) Dolomanov, O. V.; Bourhis, L. J.; Gildea, R. J.; Howard, Judith A. K.; Puschmann, H. *J. Appl. Crystallogr.* **2009**, *42* (2), 339−341.
(64) Sheldrick, G. M. *Acta Crystallogr., Sect. A: Found. Crystallogr.* **2008**, *64* (1), 112−122.
(65) Spek, A. L. *J. Appl. Crystallogr.* **2003**, *36* (1), 7−13.
(66) Frisch, M. J.; Trucks, G. W.; Schlegel, H. B.; Scuseria, G. E.; Rob, M. A.; Cheeseman, J. R.; Montgomery, J. A., Jr.; Vreven, T.; Kudin, K. N.; Burant, J. C.; Millam, J. M.; Iyengar, S. S.; Tomasi, J.; Barone, V.; Mennucci, B.; Cossi, M.; Scalmani, G.; Rega, N.; Petersson, G. A.; Nakatsuji, H.; Hada, M.; Ehara, M.; Toyota, K.; Fukuda, R.; Hasegawa, J.; Ishida, M.; Nakajima, T.; Honda, Y.; Kitao, O.; Nakai, H.; Klene, M.; Li, X.; Knox, J. E.; Hratchian, H. P.; Cross, J. B.; Bakken, V.; Adamo, C.; Jaramillo, J.; Gomperts, R.; Stratmann, R. E.; Yazyev, O.; Austin, A. J.; Cammi, R.; Pomelli, C.; Ochterski, J. W.; Ayala, P. Y.; Morokuma, K.; Voth, G. A.; Salvador, P.; Dannenberg, J. J.; Zakrzewski, V. G.; Dapprich, S.; Daniels, A. D.; Strain, M. C.; Farkas, O.; Malick, D. K.; Rabuck, A. D.; Raghavachari, K.; Foresman, J. B.; Ortiz, J. V.; Cui, Q.; Baboul, A. G.; Clifford, S.; Cioslowski, J.; Stefanov, B. B.; Liu, G.; Liashenko, A.; Piskorz, P.; Komaromi, I.; Martin, R. L.; Fox, D. J.; Keith, T.; Al-Laham, M. A.; Peng, C. Y.; Nanayakkara, A.; Challacombe, M.; Gill, P. M. W.; Johnson, B.; Chen, W.; Wong, M. W.; Gonzalez, C.; Pople, J. A. *Gaussian 03*, revision D.01; Gaussian Inc.: Wallingford, CT, 2003.
(67) Adamo, C.; Barone, V. *Chem. Phys. Lett.* **1999**, *314* (1−2), 152−157.
(68) Hay, P. J.; Wadt, W. R. *J. Chem. Phys.* **1985**, *82* (1), 270.
(69) Wadt, W. R.; Hay, P. J. *J. Chem. Phys.* **1985**, *82* (1), 284.
(70) Hay, P. J.; Wadt, W. R. *J. Chem. Phys.* **1985**, *82* (1), 299.
(71) Krishnan, R.; Binkley, J. S.; Seeger, R.; Pople, J. A. *J. Chem. Phys.* **1980**, No. 72, 650.
(72) McLean, A. D.; Chandler, G. S. *J. Chem. Phys.* **1980**, No. 72, 5639.
(73) Wachters, A. J. H. *J. Chem. Phys.* **1970**, No. 52, 1033.
(74) Lörtscher, E.; Weber, H.; Riel, H. *Phys. Rev. Lett.* **2007**, *98* (17), 176807.
(75) Barclay, J. E.; Leigh, G. J.; Houlton, A.; Silver, J. *J. Chem. Soc., Dalton Trans.* **1988**, No. 11, 2865.
(76) George, A. V.; Field, L. D.; Malouf, E. Y.; McQueen, A. E. D.; Pike, S. R.; Purches, G. R.; Hambley, T. W.; Buys, I. E.; White, A. H.; Hockless, D. C. R.; Skelton, B. W. *J. Organomet. Chem.* **1997**, *538* (1−2), 101−110.
(77) Hughes, D. L.; Leigh, G. J.; Jimenez-Tenorio, M.; Rowley, A. T. *J. Chem. Soc., Dalton Trans.* **1993**, No. 1, 75.
(78) Adams, R. D.; Davison, A.; Selegue, J. P. *J. Am. Chem. Soc.* **1979**, *101* (24), 7232−7238.
(79) Field, L. D.; George, A. V.; Laschi, F.; Malouf, E. Y.; Zanello, P. *J. Organomet. Chem.* **1992**, *435* (3), 347−356.
(80) Colbert, M. C. B.; Lewis, J.; Long, N. J.; Raithby, P. R.; Younus, M.; White, A. J. P.; Williams, D. J.; Payne, N. N.; Yellowlees, L.; Beljonne, D.; Chawdhury, N.; Friend, R. H. *Organometallics* **1998**, *17* (14), 3034−3043.
(81) Jiao, H.; Costuas, K.; Gladysz, J. A.; Halet, J.-F.; Guillemot, M.; Toupet, L.; Paul, F.; Lapinte, C. *J. Am. Chem. Soc.* **2003**, *125* (31), 9511−9522.
(82) Akita, M.; Chung, M.-C.; Sakurai, A.; Sugimoto, S.; Terada, M.; Tanaka, M.; Moro-oka, Y. *Organometallics* **1997**, *16* (22), 4882−4888.
(83) Zhuravlev, F.; Gladysz, J. A. *Chem.—Eur. J.* **2004**, *10* (24), 6510−6522.
(84) Szafert, S.; Gladysz, J. A. *Chem. Rev.* **2003**, *103* (11), 4175−4206.
(85) Forster, D.; Goodgame, D. M. L. *J. Chem. Soc.* **1965**, No. 0, 268−274.
(86) Dembinski, R.; Lis, T.; Szafert, S.; Mayne, C. L.; Bartik, T.; Gladysz, J. *J. Organomet. Chem.* **1999**, *578* (1−2), 229−246.
(87) Le Narvor, N.; Toupet, L.; Lapinte, C. *J. Am. Chem. Soc.* **1995**, *117* (27), 7129−7138.
(88) Dembinski, R.; Bartik, T.; Bartik, B.; Jaeger, M.; Gladysz, J. A. *J. Am. Chem. Soc.* **2000**, *122* (5), 810−822.
(89) Dembinski, R.; Lis, T.; Szafert, S.; Mayne, C. L.; Bartik, T.; Gladysz, J. *J. Organomet. Chem.* **1999**, *578* (1−2), 229−246.
(90) Schwarz, F.; Kastlunger, G.; Lissel, F.; Riel, H.; Venkatesan, K.; Stadler, R.; Berke, H.; Lörtscher, E. *Nano Lett.* **2014**, DOI: 10.1021/nl5029045.
(91) Goddard, W. A. *Handbook of nanoscience, engineering and technology*; CRC Press: Boca Raton, 2003.
(92) Lörtscher, E.; Elbing, M.; Tschudy, M.; von Hänisch, C.; Weber, H. B.; Mayor, M.; Riel, H. *ChemPhysChem* **2008**, *9* (15), 2252−2258.